24th International Conference on Renewable Energies and Power Quality (ICREPQ'26)
Santander (Spain), 10th to 12th June 2026
ISBN-13: 978-84-09-82044-3

Controllability of Magnetic Flux Linkages in Variable-Speed Electrically-Excited Synchronous Generators

B. Polajžer[1], A. Muetze[2], S. A. Seyed-Bouzari[2] and J. Ritonja[1]

[1] Faculty of Electrical Engineering and Computer Science
University of Maribor
Koroška cesta 46, 2000 Maribor, Slovenia, e-mail: bostjan.polajzer@um.si, jozef.ritonja@um.si

[2] Electric Drives and Power Electronic Systems Institute
Graz University of Technology
Inffeldgasse 18/1 Graz, Austria, e-mail: muetze@tugraz.at, seyedali.seyedbouzari@tugraz.at

Abstract. Synchronous generators (SGs) are the primary technology for large-scale electricity generation, with stator windings connected directly to the grid. This setup limits controllability, as control action is exerted only through rotor voltage. Variable-speed SGs, which integrate a power electronic converter between the stator and grid, enhance controllability. This paper analyzes the controllability of an electrically excited SG using a *d*-*q*-axis model of the electromagnetic subsystem, assuming that both the rotor and stator voltages are controlled. The analysis shows that the model parameters significantly affect controllability. Therefore, SG controllability can be enhanced as early as the electromagnetic design phase.

Key words. Controllability, electrically-excited SG, electromagnetic design, variable-speed system.

1. Introduction

Converter-Interfaced Synchronous Generators (CISGs) justify the increased investment costs associated with the full-size converter due to their applicability in variable-speed applications, such as pumped-hydro [1] and wind systems [2]. Given the converter-interfaced operation, new generator design solutions result in smaller volumes, reduced material costs, and enhanced efficiency [3]. Furthermore, due to their decoupled operation from the grid, CISGs can provide various services to the power grid, as required by EU Regulation 2016/63, e.g., power oscillation damping, fast fault current injection, and inertial-frequency response. Enhancing the controllability of CISGs is, obviously, of utmost importance.

CISGs are implemented as Permanent Magnet Synchronous Generators (PMSGs) in wind systems and as Electrically-Excited Synchronous Generators (EESGs) in pumped-hydro systems. This paper analyzes the controllability of magnetic flux linkages in EESGs. A *d*-*q*-axis model of the electromagnetic subsystem, represented in state-space form, is used, and the impact of variations of model parameters is studied. To evaluate the controllability of the EESG model, the energy-related controllability Gramian matrix is computed, and different Controllability Metrics (CMs) are tested [4], [5]. To present the applicability of the CMs in the electromagnetic design process, two EESG designs for hydro applications are additionally analyzed. The initial design is based on the literature and data from commercially available EESGs, while the optimized design was determined using the discussed CMs as the optimization objective.

2. Controllability Metrics for EESG

A standard model is used, considering two-phase stator (armature) windings in orthogonal magnetic axes *d* and *q*, and the rotor (field) winding in axis *d*. The damper (amortisseur) windings are not considered, as they improve stability without affecting controllability. Because stator and rotor voltages are controlled, the operating point can be maintained within the linear magnetic region, making the unsaturated model suitable for the controllability analysis [6].

The state-space matrix representation of the small-signal unsaturated model is given as $\dot{\boldsymbol{\psi}} = \mathbf{A}\boldsymbol{\psi} + \mathbf{B}\mathbf{u}$. The state vector $\boldsymbol{\psi}$ represents the flux linkages of the field winding in the *d*-axis, and armature windings in the *d*- and *q*-axes, respectively. The state matrix is given as

$$\mathbf{A} = \begin{bmatrix} -R_\mathrm{f}L_\mathrm{d}/\beta & R_\mathrm{f}L_\mathrm{afd}/\beta & 0 \\ R_\mathrm{a}L_\mathrm{afd}/\beta & -R_\mathrm{a}L_\mathrm{f}/\beta & \omega \\ 0 & -\omega & -R_\mathrm{a}/L_\mathrm{q} \end{bmatrix}, \tag{1}$$

where R_a and R_f are the resistances of the armature and field windings, respectively. Self-inductances are denoted as L_d, L_q for the armature windings, and L_f for the field winding, while L_afd denotes mutual inductance. Model also incorporates the synchronous angular speed (ω) and the term $\beta = (L_\mathrm{d}L_\mathrm{f} - L_\mathrm{afd}^2)$. The input vector $\mathbf{u}$ represents the field voltage and armature voltages in the *d*- and *q*-axes. The input matrix is the identity matrix, i.e., $\mathbf{B} = \mathbf{I}_3$, thus considering all the voltages as input variables.

The matrix pair $\{\mathbf{A},\mathbf{B}\}$ is controllable if the system inputs can drive any initial state to a desired state in finite time. The controllability Gramian matrix $\mathbf{W}_\mathrm{C}$ quantifies this property [4], and is defined as

$$\mathbf{W}_\mathrm{C} = \int_0^\infty \left((e^{\mathbf{A}t}\mathbf{B})(e^{\mathbf{A}t}\mathbf{B})^\mathrm{T} \right) dt, \tag{2}$$

where $e^{\mathbf{A}t}$ is the state-transition matrix. Two different CMs will be tested: the trace and determinant of the matrix $\mathbf{W}_\mathrm{C}$ [5]. The first CM is $\mathrm{tr}(\mathbf{W}_\mathrm{C})$, which is inversely related to the average energy required to control all directions in the state-space. Thus, a larger trace value indicates that a lower average energy is required to control the system. The second CM is $\log\det(\mathbf{W}_\mathrm{C})$ that measures the volume of reachable states with one unit or less of input energy; the logarithmic form is adopted for numerical stabilization.

3. Results

An EESG for pumped-hydro applications will be considered, with the following nominal (base) values: 345 MVA, 21 kV, 50 Hz (stator), and 220 V (field). The parameters of the small-signal model were determined using an analytic design-modelling approach [7].

The analysis of the EESG using the small-signal model will employ two sets of model parameters in p.u., corresponding to two designs, as given in Table I. The initial set of parameters was obtained from the literature and from commercially available EESGs for hydro applications. The optimized set of parameters was determined through numerical optimization using the adopted analytic design-modelling approach, with the objective based on $\mathrm{tr}(\mathbf{W}_\mathrm{C})$. It should be noted that the optimized design using $\log\det(\mathbf{W}_\mathrm{C})$ resulted in a practically identical EESG design. The self-inductance L_d was fixed during the optimization.

Table I. Initial and optimized sets of the small-signal model parameters (p.u.).

design	initial	optimized
R_a	0.0026	0.0019
R_f	0.00046	0.00025
L_d	1.2	1.2
L_q	0.867	0.924
L_f	1.238	1.826
L_afd	1.049	0.871

A. Impact of Small-Signal Model Parameters on Controllability

Considering only the initial set of small-signal model parameters (see Table I), each parameter was varied from its initial value to demonstrate its impact on the CMs. The results are presented in Figs. 1-6, where the circle markers indicate the initial CM values obtained from the initial set of model parameters. Furthermore, the synchronous angular speed ω was also varied from 0.1 to 1 p.u., and the results show that it does not affect the CMs.

Figs. 1 and 2 show the impact of winding resistances, which are inversely related to both CMs. Such a relationship is inherent, as larger resistances increase copper losses, thus more energy is required to control the system's state. Consequently, EESGs with smaller winding resistances are more controllable. Results also show that $\mathrm{tr}(\mathbf{W}_\mathrm{C})$ is more affected by the variation of R_f, while $\log\det(\mathbf{W}_\mathrm{C})$ is more affected by the variation of R_a.

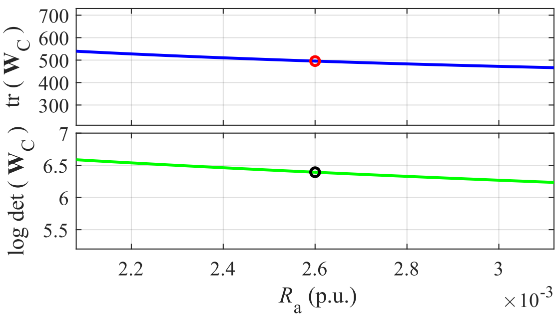

Fig. 1. Impact of armature winding resistance variation on CMs.

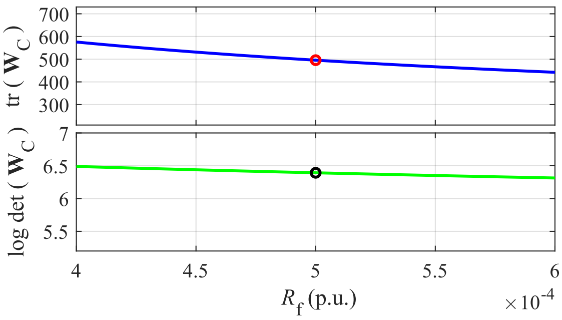

Fig. 2. Impact of field winding resistance variation on CMs.

The impact of variation in inductances on CMs is not as straightforward as that of variation in winding resistances. Fig. 3 shows the impact of the d-axis self-inductance variation, where the ratio $L_\mathrm{d}/L_\mathrm{q}$ was kept constant. Thus, L_d and L_q were both simultaneously varied. Results show an almost linear relationship with $\mathrm{tr}(\mathbf{W}_\mathrm{C})$ and $\log\det(\mathbf{W}_\mathrm{C})$. Note that the same relationship was also found when $L_\mathrm{d}/L_\mathrm{q}$ was not kept constant. The impact of the q-axis self-inductance variation on CMs in Fig. 4 also shows an almost linear relationship with $\log\det(\mathbf{W}_\mathrm{C})$, and $\mathrm{tr}(\mathbf{W}_\mathrm{C})$; however, the impact of variation in L_q is small.

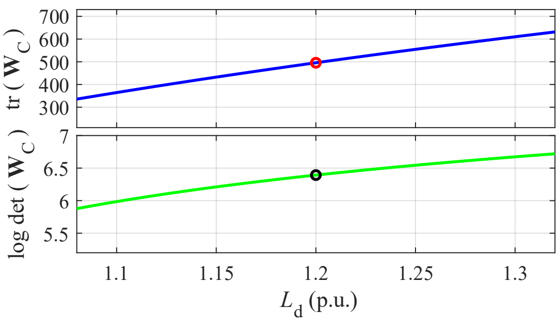

Fig. 3. Impact of armature winding d-axis self-inductance variation on CMs, where $L_\mathrm{d}/L_\mathrm{q} = \mathrm{const}$.

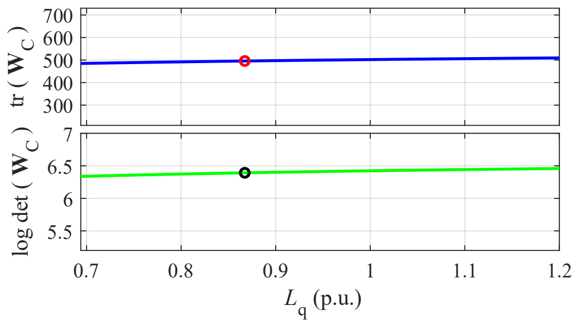

Fig. 4. Impact of armature winding q-axis self-inductance variation on CMs, where $\max(L_\mathrm{q}) = L_\mathrm{d}$.

Fig. 5 shows the impact of the field winding self-inductance variation on both CMs, which is qualitatively and quantitatively similar to the impact of the armature winding d-axis self-inductance variation (see Fig. 3). The impact of mutual inductance variation on CMs is exactly the opposite, as shown in Fig. 6. Moreover, among all the parameter variations, variation in L_afd shows the largest impact on both CMs, $\mathrm{tr}(\mathbf{W}_\mathrm{C})$ and $\log\det(\mathbf{W}_\mathrm{C})$.

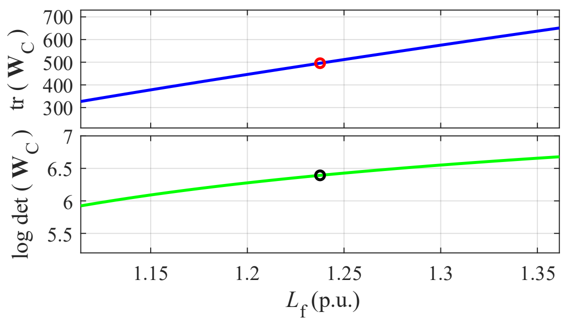

Fig. 5. Impact of field winding self-inductance variation on CMs.

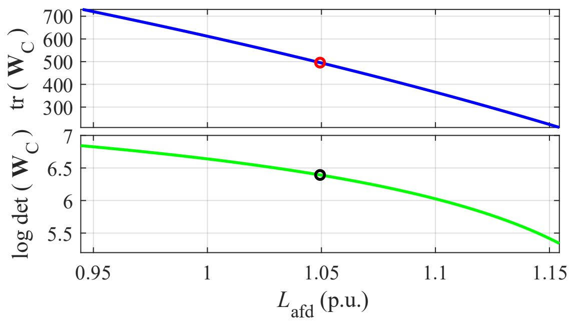

Fig. 6. Impact of mutual inductance variation on CMs.

B. Analysis of Small-Signal Model Parameters and Design Variables

The initial and optimized EESG designs are analyzed (see Table I). Compared to the initial design, the values of R_a and R_f are lower in optimized design, while the values of L_q and L_f are higher. It should be noted that L_d was fixed, so the two designs have the same value. Furthermore, the value of L_afd in the optimized design is lower than that of the initial design. These relationships are consistent with the results shown in the previous Section (see Figs. 1-6).

Furthermore, Table II lists the design variables that were used in the design-modelling process, such as the number of pole pairs (p), the magnetic flux densities in the air gap and in the stator yoke (B_ag and $B_\mathrm{s-yoke}$), and the stator and rotor current densities (j_s and j_r). Several geometric ratios were also used, i.e., stack length / pole pitch (λ_m), stator slot width / slot pitch ($K_\mathrm{s-slot}$), rotor pole-shoe width / pole pitch ($K_\mathrm{r-sw}$), rotor pole-shoe height / pole pitch ($K_\mathrm{r-sh}$), rotor pole-body width / pole pitch ($K_\mathrm{r-bw}$), rotor pole-body height / pole pitch ($K_\mathrm{r-bh}$), and rotor yoke height / pole pitch ($K_\mathrm{r-yoke}$).

The results for both EESG designs given in Table II show that, compared to the initial design, the optimized design has a lower p, while B_ag and $B_\mathrm{s-yoke}$ are slightly lower, whereas j_s and j_r are significantly lower. Furthermore, λ_m of the optimized design is significantly lower, while the ratios $K_\mathrm{s-slot}$, $K_\mathrm{r-sw}$, $K_\mathrm{r-sh}$, and $K_\mathrm{r-bh}$ are higher. The ratios, $K_\mathrm{r-yoke}$ and $K_\mathrm{r-bw}$ remain practically unchanged. Let us also emphasize that both designs have the same efficiency of 98%, whereas the optimized design has a higher power density than the initial design.

Table II. Design variables for the initial and optimized EESG designs.

design	initial	optimized
p	8	6
B_ag (T)	0.85	0.801
$B_\mathrm{s-yoke}$ (T)	1.2	1.095
j_s (A/mm^2)	5	3.004
j_r (A/mm^2)	5	3.002
λ_m	2.5	0.637
$K_\mathrm{s-slot}$	0.4	0.454
$K_\mathrm{r-sw}$	0.7	0.8
$K_\mathrm{r-sh}$	0.1	0.2
$K_\mathrm{r-bw}$	0.5	0.5
$K_\mathrm{r-bh}$	0.3	0.55
$K_\mathrm{r-yoke}$	0.3	0.322

Moreover, Table III shows CMs for the two discussed designs. Compared to the initial design, the $\mathrm{tr}(\mathbf{W}_\mathrm{C})$ is increased by a factor of 5.7, while the $\log\det(\mathbf{W}_\mathrm{C})$ is increased by 1.68.

Table III. CMs for initial and optimized sets of the small-signal model parameters.

design	initial	optimized
$\mathrm{tr}(\mathbf{W}_\mathrm{C})$	496	2835
$\log\det(\mathbf{W}_\mathrm{C})$	6.39	8.07

C. Time-Domain Simulations

This Section aims to support the analysis of the CMs by time-domain simulations. The initial values of the armature (stator) voltages were set to $u_\mathrm{d}(0) = -0.5$ p.u. and $u_\mathrm{q}(0) = 1$ p.u., while the initial value of the field (rotor) voltage was set to $u_\mathrm{f}(0) = 0.0005$ p.u. All voltages were step-wise increased by 10%, but with different time delays. First u_f was changed at 18.75 s, then u_q at 75 s, and finaly u_d at 112.5 s.

The following quantities were observed over time: (i) the norm of the stator (armature) magnetic flux linkage vector $\|\psi_a\| = \sqrt{\psi_d^2 + \psi_q^2}$, (ii) the back emf $e_a = (\omega L_{afd} i_f)$, where i_f is the field winding current, and (iii) the absolute value of the instantaneous apparent power $|s| = \|u_a\|\|i_a\|$, where $\|u_a\| = \sqrt{u_d^2 + u_q^2}$ and $\|i_a\| = \sqrt{i_d^2 + i_q^2}$ are the norms of the stator (armature) voltage and current vectors, respectively.

Two sets of small-signal model parameters, as given in Table I, were used to compute time-domain simulations numerically. Fig. 7 shows the resulting instantaneous responses over time, where the nominal synchronous angular speed was used ($\omega = 1$ p.u.). The time was denormalized using the base value $T_b = 1/\omega_b$, where $\omega_b = 2\pi f_N$ and $f_N = 50$ Hz. For the same input voltages, the resulting back emf and apparent power are considerably higher for the optimized design.

Furthermore, as shown in Fig. 7, the optimized design exhibits longer time constants and lower oscillation damping. Table IV also shows the time constants and the damping ratio computed from the eigenvalues of the state matrix given by (1). All three eigenvalues have negative real parts, indicating stability. One eigenvalue is real and corresponds to the non-oscillatory rotor (field winding) mode, which is characterized by a time constant T_r. Two eigenvalues are conjugate complex and correspond to the oscillatory stator (armature winding) mode. This mode has a time constant T_s, a frequency of oscillations equal to the synchronous angular speed ω, and the damping ratio ζ_s.

Table IV. Time constants and the damping ratio.

design	initial	optimized
T_r (s)	2.036	15.202
T_s (s)	0.559	1.422
ζ_s	0.0057	0.0022

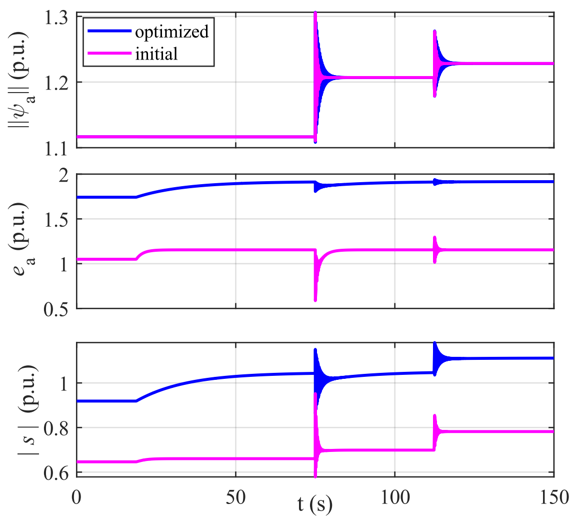

Fig. 7. Stator magnetic flux linkage, back emf, and apparent power over time during changes in u_f at 18.75 s, in u_q at 75 s, and in u_d at 112.5 s, and $\omega = 1$ p.u..

4. Conclusion

This paper presents a controllability analysis of two electromagnetic design options of the 345 MVA EESG for pumped-hydro applications. A small-signal model was used, and controllability was analyzed using two energy-related CMs. The main conclusions are as follows:

1. Winding resistances are inversely related to both CMs. Self-inductances are almost linearly related to both CMs, while the relationship between the mutual inductance and both CMs is exactly the opposite.
2. The CMs discussed were used as objectives in the analytic-design modelling approach. The resulting optimized designs have almost identical parameters.
3. Compared to the initial EESG design, the optimized design has lower winding resistances, higher self-inductances, and a lower mutual inductance.
4. Both the initial and optimized EESG designs have the same efficiency, but the optimized design has a higher power density.
5. The optimized EESG exhibits a longer time constant and lower damping of the oscillatory stator mode, while the time constant of the non-oscillatory rotor mode is considerably longer.

Future work will detail the adopted analytic design-modelling approach. Modal analysis will be fully incorporated in the electromagnetic design process to constrain the time constants and damping of optimized solutions. The evolution of design variables from initial to optimized values will also be investigated, along with a physical interpretation of these changes on EESG configurations.

References

[1] M. Valavi, A. Nysveen, "Variable-Speed Operation of Hydropower Plants: A Look at the Past, Present, and Future", IEEE Industry Applications Magazine (2018), vol. 24, no. 5, pp. 18–27.

[2] H. Chen, et al., "Modern electric machines and drives for wind power generation: A review of opportunities and challenges", IET Renewable Power Generation (2021), vol. 15, pp. 1864–1887.

[3] T. Holzer, et al., "Generator Design Possibilities for Full-Size Converter Operation of Large Pumped Storage Power Plants," IEEE Transactions on Industry Applications (2020), vol. 56, no.4, pp. 3644–3655.

[4] C.-T. Chen, Linear System Theory and Design, 3rd ed. Oxford: Oxford University Press, New York (1999).

[5] T. H. Summers, F. L. Cortesi and J. Lygeros, "On submodularity and controllability in complex dynamical networks," IEEE Transactions on Control of Network Systems (2016), vol. 3, no. 1, pp. 91–101.

[6] J. H. Stavnesli and J. K. Nøland, "Stator Flux-Regulatory Excitation Control in Converter-Fed Synchronous Machines for Pumped-Storage Variable-Speed Hydropower," IEEE Open Access Journal of Power and Energy (2022), vol. 9, pp. 340–350.

[7] G. Müller, Berechnung Elektrischer Maschinen, (2007).